

GRB 050822: Detailed analysis of an XRF observed by *Swift*

O. Godet¹, K. L. Page¹, J. Osborne¹, B. Zhang², D. N. Burrows⁴, P. T.
O’Brien¹, J. E. Hill³, J. Racusin⁴, A. P. Beardmore¹, M. R. Goad¹, A. Falcone⁴,
D. C. Morris⁴, H. Ziaeeepour⁵

¹ X-ray and Observational Astronomy Group, Department of Physics &
Astronomy, University of Leicester, LE1 7RH, UK

² Department of Physics, University of Nevada, Box 454002, Las Vegas, NV 89154-
4002, USA

³ NASA Goddard Space Flight Center, Greenbelt, MD 20771, USA

⁴ Department of Astronomy & Astrophysics, 525 Davey Lab, Pennsylvania State
University, University Park, PA 16802, USA

⁵ INAF-Osservatorio Astronomico di Brera, Via E. Bianchi 46, 23807, Merate
(LC), Italy

⁵ Mullard Space Science Laboratory, University College London, Holmbury St.
Mary, Dorking Surrey, RH5 6NT, UK

Received : / Accepted :

Abstract.

We report on the temporal and spectral characteristics of the early X-ray emission from the GRB 050822 as observed by *Swift*. This burst is likely to be an XRF showing major X-ray flares in its XRT light-curve. The quality of the data allows a detailed spectral analysis of the early afterglow in the X-ray band. During the X-ray flares, a positive correlation between the count rate and the spectral hardness (i.e. higher the count rate is and harder the spectrum is) is clearly seen for the X-ray flares. This behaviour similar to that seen for Gamma-ray pulses indicates that the energy peak of the spectrum is in the XRT energy band and it moves at lower energy with time. We show evidence for the possible detection of the emergence of the forward-shock emission produced at a radius larger than 4×10^{16} cm (a forming region clearly different to that producing the prompt emission). Finally, we show that the null detection of a jet break up to $T_0 + 4 \times 10^6$ s in the X-ray light curve of this XRF can be understood: i) if the jet seen on-axis is uniform with a large opening angle ($\theta > 20^\circ$); or ii) if the jet is

a structured Gaussian-like jet with the line-of-sight outside the bright Gaussian core.

Key words. gamma-ray: bursts – Gamma-rays, X-rays: individual (GRB 050822), energy peak, XRF, thermal component

1. Introduction

X-ray flashes (XRFs) and X-ray rich Gamma-ray bursts (XRR GRBs) first detected by *Ginga* and BeppoSAX (e.g. Heise et al. 2001) emit most of their prompt energy in X-rays (see Lamb et al. 2004). It has been shown that XRFs and GRBs share many observational properties, including: i) the temporal and spectral properties of the prompt emission (e.g. Heise et al. 2001, Kippen et al. 2003, Sakamoto et al. 2005); ii) host galaxy properties (e.g. Bloom et al. 2003); iii) broadband afterglows as observed by *Swift* (Gehrels et al. 2004 - XRFs 050215B, Levan et al. 2006a; 050315, Vaughan et al. 2006; 050406, Romano et al. 2006; 050416A, Mangano et al. 2006; 050714B, Levan et al. 2006b; 060218, Campana et al. 2006b). The association of XRFs with supernovae of type Ib/c (e.g. Tominga et al. 2004, Thomson et al. 2004, Watson et al. 2004) suggests that XRFs and long GRBs share a similar progenitor. Thus, it has been proposed that XRFs are simply an extension of the long-GRB population with low values of the energy peak (E_p) of the prompt spectra (e.g. Sakamoto et al. 2005, Barraud et al. 2003).

A number of theoretical models have been proposed to explain XRFs. Some are based on intrinsic physical differences in the jet outflow (e.g. Mizuta et al. 2006) or in the jet geometries between XRFs and GRBs. Thus, the “dirty fireball” invokes entrainment of baryonic material in the GRB jet, resulting in a bulk Lorentz factor $\Gamma \ll 300$ (e.g. Dermer et al. 1999, Huang et al. 2002, Dermer & Mitman 2004). Mochkovitch et al. (2004) alternatively have proposed that GRB jets, in which the bulk Lorentz factor $\Gamma > 300$ and the contrast between the bulk Lorentz factors of the colliding relativistic shells are small, can also produce XRFs. It also has been proposed that XRFs could simply have an intrinsically wider jet opening angle in the case of a uniform jet model, since the energy peak of GRB spectra is anti-correlated with the jet opening angle (Lamb et al. 2005; see also Li et al. 2006).

On the other hand, other models simply invoke an effect of the viewing angle. Indeed, Mészáros et al. (2002) have stressed that X-ray photons could be produced by the view of the cocoon surrounding the GRB jet as it breaks out, instead of the narrow jet (also see Zhang, Woosley & Heger 2004). Another interesting model based on the unification scheme of AGN speculates that XRFs could be the result of a highly collimated GRB jet viewed off the jet axis (Yamazaki et al. 2003, Zhang et al. 2004).

The recent *Swift* broadband observations of XRFs have shown a variety of temporal and spectral behaviour. In the case of the peculiar event 060218, it was established that the explosion was quasi-isotropic (Soderberg et al. 2006). Similarly, Mangano et al. (2006) have shown that the jet opening angle of GRB 050416A could be much larger ($\theta > 20^\circ$) than those derived for GRBs ($5 - 10^\circ$, e.g. Frail et al. 2001). On the other hand, the light curve of GRB 050315 (Vaughan et al. 2006) shows evidence for a possible jet break at 2.5×10^5 s, implying a jet opening angle of 5° , consistent with the values derived for GRBs. Finally, XRF 050406 has been shown to be a burst possibly seen well off the axis of a structured jet (Schady et al. 2006).

These results suggest that the origin of XRFs is still not settled. It is therefore important to study the XRF-like events in detail to constrain their true origins.

Here, we report the case of a burst detected by the *Swift* BAT (Burst Alert Telescope; Barthelmy et al. 2005) on 22nd August 2005. The X-ray light curve of this event exhibits a steep-to-flat-to-steep decay, and large X-ray flares are superposed on the initial steep underlying decay. We show that one of the X-ray flares could present a quasi-thermal component. The paper is organised as follows: in Section 2, we present the characteristics of the observations and the basic steps of the data reduction. In Section 3, we present the temporal and spectral analysis of the multi-wavelength observations. We establish that this burst is probably an XRR GRB or an XRF, by using the BAT spectral results to compute the softness ratio (e.g. Lamb et al. 2004). In Section 4, we investigate the physical mechanisms producing the spectral and temporal characteristics of the burst.

By convention, we note hereafter the flux in the X-ray band is modelled as $F_\nu \propto \nu^{-\beta}(t - T_0)^{-\alpha}$, where β is the energy spectral index, α is the temporal index, and T_0 is the BAT trigger time. We use the symbol Γ to refer to the bulk Lorentz factor. The BAT spectral slope is noted as β_{BAT} . All the time intervals are hereafter referenced to the BAT trigger time.

2. Observation and data reduction

2.1. BAT observations

The burst 050822 (*Swift*-BAT trigger 151486) was detected at 03:49:29 UT on 22nd August 2005 at (J2000) RA= $03^{\text{h}}24^{\text{m}}19^{\text{s}}$ and Dec= $-46^{\text{d}}01'22''$, with an uncertainty of 2 arc-minutes (Blustin et al. 2005).

The BAT spectra and light curves were extracted using the BAT analysis software (build 2.3) as described in the *Swift* BAT Ground Analysis Software Manual (Krimm, Parsons & Markwardt 2004).

2.2. XRT observations

The X-Ray Telescope (XRT, Burrows et al. 2005) started to observe the burst 95 s after the trigger, following the sequence of readout modes: Image mode (IM) at the end of the slew, Windowed Timing (WT), and then Photon Counting (PC) modes while pointed at the target (Hill et al. 2004, 2005). The Low Rate Photo-Diode mode is no longer used, since the XRT CCD detector was damaged by a micro-meteoroid on 27th May 2005 producing several bad columns (Abbey et al. 2005). The XRT observations are summarised in Table 1. Note that the X-ray light curve needs to be corrected for the loss of counts, because the source is located on the CCD chip close to the bad columns. To do that, we fit the profile of the XRT point spread function (PSF, Moretti et al. 2005) to estimate the fraction of lost counts in the IM data and the first orbit of the WT and PC data (i.e. before $T_0 + 1000$ s). The correction factor applied to the X-ray light curve before $T_0 + 1000$ s is $f \sim 1.22$.

An uncatalogued X-ray source was identified at (J2000) RA = $03^{\text{h}}24^{\text{m}}27.26^{\text{s}}$ and Dec = $-46^{\text{d}}02'00.3''$ with an uncertainty of $1.4''$ at a 90% confidence level. This refined ground-calculated position was obtained after astrometry corrections. To do so, we remove the first 100 s of each orbit where the star tracker attitude was less stable. For GRB 050822, this leaves only 216 ks of PC data. The data are further filtered to remove any remaining hot pixels that are not filtered out by the normal pipeline processing, then exposure maps are made based on the remaining data, and all images and exposure maps are summed. We obtain all of the optical objects within $15'$ from either SDSS if available or USNO-B1 if not. In the case of GRB 050822 we use USNO-B1. To find serendipitous X-ray sources for matching, we run WAVDETECT on the combined XRT image, and then run XRTCENTROID to get the best positions taking into account the instrument PSF and exposure maps. We do not do individual object to object matching, but rather we match all X-ray sources to all optical sources and grab all matches with a separation less than $20''$. We look for clustering in those matches to find the overall mean frame shift. We find the weighted mean frame shift measured from all the matches and remove all outliers further away than 2σ from the mean. We then iterate finding the mean and removing outliers for a few more iterations also requiring only one match per X-ray source on the third iteration. Finally, we take this mean shift and apply it to the GRB position. We calculate the statistical position errors using the empirical fits as described in Moretti et al. (2006), assuming that the astrometry correction removes the $3.5''$ systematic error normally applied to XRT positions to account for errors in the star tracker attitude solution. We add the statistical error to the error from the frame shift due to the counting on each individual serendipitous source. We note that our best XRT position is $0.5''$ away from the astrometry corrected position (RA(J2000)= $03^{\text{h}}24^{\text{m}}27.22^{\text{s}}$,

Dec(J2000) = $-46^{\circ}02'00.0''$ with an uncertainty of $0.7''$ at 90% confidence level) given for this burst by Nat Butler (2006).

The XRT data were processed by the *Swift* software version 2.5¹. This software release includes new response files for the PC and WT modes which significantly improves the spectral response at low energy (below 0.7 keV). It is now possible to extend the fits down to 0.3 keV in both modes (Campana et al. 2006a). The residuals below 0.6 keV are better than 10% and the flux accuracy between the PC and WT modes are better than 5%. A cleaned event list was generated using the default pipeline, which removes the effects of hot pixels and the bright Earth. From the cleaned event list, the source and background spectra were extracted using XSELECT.

Due to pile-up in the IM data, only the WT and PC data were useful for spectral analysis. The PC data from ~ 354 s to ~ 414 s and from ~ 617 s to ~ 690 s with a count rate above 1 count s^{-1} are moderately piled-up. The innermost four-pixel radius was excluded, and the source and background spectra were extracted using an annular region with an outer radius of 20 pixels. The same annular region was used to correct the pile-up effect in the PC data for the X-ray light curve. For the spectral and temporal analysis, we used the grade 0-12 events for the PC mode and the grade 0-2 events for the WT mode, giving slightly higher effective area at higher energies. The ancillary response files for the PC and WT modes were created using XRTMKARF.

2.3. UVOT and other optical observations

UVOT (UV-Optical Telescope; Roming et al. 2005), which began to observe 138 s after the trigger, detected no optical fading source down to a 3σ limiting magnitude of 19.5 in V-band for a 278 s exposure and 19.4 in U-band for a 188 s exposure (Page et al. 2005).

ROTSE-III (Rykoff et al. 2005) started to observe 31.7 s after the trigger (i.e. during the Gamma-ray prompt emission phase), but no source was detected down to an unfiltered magnitude of 16.6 in a 84 s (at $T_0 + 31.7$ s) co-added images exposure, and 17.5 in a 246 s ($T_0 + 412.6$ s) co-added images exposure.

No redshift information is available for this event.

3. Data analysis

All the errors cited below are given at a 90% confidence level for one parameter of interest (i.e. $\Delta\chi^2 = 2.706$).

¹ See <http://heasarc.gsfc.nasa.gov/docs/swift/analysis/>

3.1. Spatial Analysis

Fig. 1 shows a 0.2-10 keV Photon Counting image of the sky region around GRB 050822 accumulated over 256 ks. The image is smoothed using a Gaussian with a value of the kernel radius fixed at 2. A nearby faint X-ray source (SX) was detected at (J2000) RA=03^h24^m22.37^s and Dec=−46^d02′10.55″ with a 90% error radius of 2.3″ using the same method described in Section 2.2. This source is 4.9″ away from the X-ray counterpart of GRB 050822. A possible optical counterpart to SX (1.5″ away from the SX position) is found in the catalogue USNO-B1.0 (RA(J2000) = 03^h24^m22.37^s, Dec(J2000)=−46^d02′12.0″; Monet et al. 2003).

Fig. 2 shows the X-ray light curve of this nearby source in the 0.2-10 keV energy band from $\sim 5 \times 10^4$ s to $\sim 5 \times 10^6$ s using a 15 pixel-radius extraction region. With a mean count rate of $\sim 10^{-3}$ counts s^{−1}, the source does not contaminate the light curve of GRB 050822 before $\sim T_0 + 3 \times 10^5$ s.

While counts from GRB 050822 dominated the field, a 20 pixel radius was used to extract the light curve and spectra, to avoid any contamination from the serendipitous source. After $T_0 + 5 \times 10^4$ s, a 15 pixel extraction radius was used.

3.2. Light curve

3.2.1. Gamma-ray band

GRB 050822 exhibits a complex multi-peaked light curve (see Fig. 3), with peaks at $T_0 + \sim 0$ s, ~ 42 s, ~ 48 s and $\sim 55 - 60$ s. A small peak between ~ 100 s and ~ 104 s can be also seen in the BAT light curve in the 15-25 keV and 25-50 keV energy bands. A faint tail or flare from ~ 104 s to ~ 200 s can be also seen by eye (see the small window in the top panel in Fig. 3). Above 100 keV, only weak emission is seen in the BAT light curve.

T_{50} and T_{90} in the 15-350 keV band are 43.9 ± 0.2 s and 104.7 ± 0.4 s, respectively.

3.2.2. X-ray band

GRB 050822 shows a complex XRT light curve in the 0.3-10 keV energy band (see the top panel in Fig. 4). The first 1000 s of data display at least three major X-ray flares peaking at ~ 131 s (F_1), ~ 236 s (F_2) and ~ 420 s (F_3) superposed on an underlying decay.

Hereafter, we use the symbols F_n to refer to these X-ray flares. Note that the rise of the flare F_3 is relatively fast with a timescale less than 30 s. After $\sim 800 - 900$ s, the light curve shows a flat-to-steep decay similar to that seen in other *Swift* bursts.

The bottom panel of Fig. 4 shows a hardness ratio, defined as the ratio of the 1-10 keV band to the 0.3-1 keV band, as a function of time. Some spectral hardening and softening

are clearly seen during the rising and decaying parts of the X-ray flares, respectively, for the flares peaking around $T_0 + 236$ s (F_2) and 420 s (F_3), and a clear spectral softening is seen for the decay of the X-ray flare peaking at $T_0 + 131$ s (F_1) (the observation began during this flare).

We note that the X-ray and Gamma-ray emission during the temporal BAT/XRT overlap are likely to be produced by the same mechanism (see Fig. 4 and Section 3.3.2). These clues suggest that the global decay seen before 1000 s could be the result of curvature effect emission (e.g. Kumar & Panaitescu 2000 and Dermer 2004) associated with each X-ray flare. This is confirmed by Liang et al. (2006; see Figure 1 and also Table 1 in their paper).

After 800-900 s, the light curve can be described by a broken power-law with an initial shallow slope $\alpha_1 = 0.45^{+0.12}_{-0.11}$ followed after a break at $1.7^{+0.5}_{-0.2} \times 10^4$ s by a steeper slope ($\alpha_2 = 1.05 \pm 0.05$) with a possible late X-ray flare peaking at $\sim 1.1 \times 10^5$ s (see Fig. 4).

3.3. Spectroscopy

3.3.1. Gamma-ray band

The BAT spectra are well fit by a single power-law. All the spectral parameters and the fluence for different time intervals are summarised in Table 2. The use of a Band function (Band et al. 1993) or a cutoff power-law model did not significantly improve the fit. The 15-150 keV fluence GRB 050822 is $2.3^{+0.2}_{-0.3} \times 10^{-6}$ erg cm $^{-2}$ over T_{90} , which is moderate when compared to the average BAT fluence of 3.1×10^{-6} erg cm $^{-2}$ for GRBs from January 2005 to September 2006. The spectral slopes of GRB 050822 are relatively steep with respect to the average BAT spectral slope of ~ 0.8 (e.g. O'Brien et al. 2006). This suggests that E_p may be below the BAT energy band, and that this burst may be an XRF or an XRR GRB.

Classification of a burst as an XRF or an XRR GRB depends on the softness ratio of the 2-30 keV fluence over the 30-400 keV fluence (e.g. Lamb et al. 2004). Bursts with $SR > 0$ are classified as XRFs, bursts with $-0.5 < SR < 0$ are classified as XRR GRBs, and those with $SR < -0.50$ are classified as normal GRBs. Because the BAT is not sensitive over this entire energy range, we compute $SR = \log \frac{S_X(2-30 \text{ keV})}{S_\gamma(30-400 \text{ keV})}$ by integrating the best-fit spectra over these energy ranges.

If we assume that the energy peak E_p is below 2 keV, we find $SR \sim 0.6$, corresponding to an XRF. On the other hand, if we assume $E_p = 15$ keV and $\beta_{\text{Band}} = 0$ (which is the mean value of the low energy spectral index of the Band function for GRBs and XRFs; Preece et al. 2000, Kippen et al. 2003), we find $SR = -0.15$, in the XRR range. Note that a smaller β_{Band} -value would result in a higher value of SR . So, the burst 050822 is likely to be an XRF or an XRR GRB.

3.3.2. X-ray band

The Galactic column density is $N_H^{Gal} = 2.34 \times 10^{20} \text{ cm}^{-2}$ in the direction of this burst (Dickey & Lockman 1990). All the spectra were binned to contain more than 20 cts bin^{-1} , and were fit from 0.3 to 10 keV within XSPEC v11.3.1 (Arnaud 1996), except when the statistics were too low, and in these cases, Cash statistics were used (Cash 1979). To model the absorption within XSPEC, we used the photo-electric absorption model (WABS).

BAT/XRT analysis - To investigate whether the early X-ray emission is connected to the Gamma-ray emission, we fit the BAT and WT spectra from 111 s to 125 s with an absorbed power-law. We did not use the BAT data beyond 125 s because of poor statistics, and useful spectral data started to be taken with the XRT only from 111 s (see Section 2.2). A single absorbed power-law gives a good fit with a slope of $\beta = 0.97_{-0.13}^{+0.14}$ and an excess absorption value of $\Delta n_H(z=0) = 1.8 \pm 0.4 \times 10^{21} \text{ cm}^{-2}$ over the Galactic value ($\chi^2/\nu = 100/108$) using a constant factor ($f = 0.95 \pm 0.10$) to take into account the difference in calibration between the XRT and the BAT (see Fig. 5). The use of an absorbed cutoff power-law or a broken power-law did not significantly improve the fit. This result is consistent with the hypothesis that the X-ray and Gamma-ray emissions are produced by the same mechanism during this time interval, and suggest that E_p must be outside the energy band 0.5-150 keV (and presumably below this band, given the high spectral index).

XRT analysis - The fit of the WT data from 111 s to 616 s using an absorbed power-law with absorption fixed to the Galactic value is poor with $\chi^2/\nu = 1743/264$. Leaving the absorption component free significantly improves the fit with $\chi^2/\nu = 362/255$, with excess absorption of $\Delta n_H(z=0) = 1.4 \pm 0.1 \times 10^{21} \text{ cm}^{-2}$ over the Galactic value. Adding a black-body component further improves the fit by ($\Delta\chi^2 = 124$ for 2 DOF), and obtains an excess absorption column of $\Delta n_H(z=0) = 9.5_{-1.9}^{+2.0} \times 10^{20} \text{ cm}^{-2}$. A consistent value of excess absorption ($\Delta n_H(z=0) = 1.2 \pm 0.4 \times 10^{21} \text{ cm}^{-2}$) is found when the PC data from ~ 800 s to $\sim 4.1 \times 10^4$ s are fit using an absorbed power-law.

Hereafter, we used two WABS models in XSPEC with one fixed to the Galactic value, and for the other, we take the more reliable Δn_H -value of $1.2 \times 10^{21} \text{ cm}^{-2}$. Indeed, the Δn_H -value derived from the WT data could be biased due to the significant spectral evolution seen in the WT data (see the bottom panel in Fig. 4 showing the hardness ratio (HR) of the 1-10 keV energy band over the 0.3-1 keV energy band from 111 s to 10^6 s), while most of the data used for the PC spectrum from ~ 800 s to $\sim 4.1 \times 10^4$ s do not show such a significative spectral evolution.

We divided the WT data into 17 segments in order to investigate the spectral evolution seen during the flares (§3.2.2) and the origin of the apparent thermal component. We obtained WT mode spectra from six time intervals for flare F_1 (111-211 s), four intervals for flare F_2 (211-351 s), and 7 intervals for flare F_3 (417-616 s). Flare F_3 also includes

some PC mode data, because the count rate following flare F_2 dropped below the PC mode threshold briefly before the rise of flare F_3 switched XRT back into WT mode. All the best-fit spectral parameters and fluxes for each time interval are summarised in Table 3. Note that the unabsorbed fluxes given in Table 3 are corrected for the effect of the bad columns using a new tool XRTEXPOMAP 0.2.1 implemented in the version 2.4 of the XRT software. We will discuss each flare in turn.

The six spectra for flare F_1 are well-fit with a single power-law spectral model (Table 3). The spectral slopes steepen with time, in agreement with the hardness ratio (Fig. 4). Using a broken power-law² does not allow us to constrain the evolution of energy peak of the spectrum (E_p) with time. These points, along with the evidence that the X-ray and Gamma-ray spectra from 111 s to 125 s are likely to be produced by the same mechanism, suggest that E_p has probably already passed through the XRT energy band by $T_0 + 111$ s.

The WT spectrum extracted for flare F_2 (from 211 s to 301 s post-burst) is not well fit by an absorbed power-law, with $\chi^2/\nu = 42.9/29$. Since we have evidence that the X-ray flares are produced by the same radiation mechanism producing the Gamma-ray peaks, we considered fitting this spectrum with a Band function (Band et al. 1993). However, the narrow 0.3-10 keV XRT energy band does not allow us to constrain the spectral parameters of the Band function with the available statistics. Instead, we approximated the Band function with an absorbed broken power-law model, where β_1 and β_2 are the low energy and high energy spectral slopes, respectively. In order to obtain constraints on the other model parameters, we assume β_1 to be 0 (the mean Band function low energy spectral slope for BATSE bursts), and obtain a good fit for the overall spectrum of flare F_2 ($\chi^2/\nu = 20/28$) with $\beta_2 = 1.95 \pm 0.17$. To track the evolution of E_p during this flare, we fit the first three spectral slices (WT7-WT9) with the same model: an absorbed broken power-law with β_1 fixed to 0. Table 3 shows that we obtained only upper limits for E_p for spectra WT7 and WT9. The spectrum WT10 of the WT data from 301 s to 351 s is best fit by a single absorbed power-law with $\beta \sim 2$, which is consistent with the β_2 -value of the broken power-law model. Although we were able to measure E_p only for spectrum W8, it is not completely clear whether E_p varies during this flare. The results suggest that, like flare F_1 , E_p was below the XRT band for most of flare F_2 .

The average spectrum of flare F_3 (from 417 s to 616 s), like that of flare F_2 , is not well fit by a single absorbed power-law, with $\chi^2/\nu = 678/135$. An absorbed broken power-law gives a good fit ($\chi^2/\nu = 141/133$). We used this spectral model for the PC spectrum from 355 to 415 s as well as the seven WT spectral slices, allowing us to track

² Note that within the XSPEC notations, the energy break (E_b) is one of the three parameters of the broken power-law model. We refer to E_b in the text as the energy peak of the spectrum (E_p).

the decrease of the peak energy with time during the flare (see Table 3 and Fig 6). For these spectra, we fit both β_1 and β_2 , although they were tied to the same values for all eight spectra. Although E_p was well determined during the bulk of this flare, it was not constrained at all for the PC spectrum from 625s to 789s at the end of the flare. When the spectrum from this time interval is fit by a single absorbed power-law, the spectral slope is still inconsistent with the β_2 -value derived from the earlier WT spectra (see Table 3). The presence of an extra X-ray emission component at this time could account for this inconsistency. This assumption is supported by the spectral hardening seen after $\sim T_0 + 700$ s in Fig. 4 (also see Section 4.3 for a discussion about the origin of this spectral hardening).

Alternatively, the average spectrum of flare F₃ can be fit using a black-body (BB) + power-law (PL) model, which was used previously in the case of GRB 060218 (Campana et al. 2006b), with $kT = 0.185^{+0.007}_{-0.006}$ keV, $\beta = 2.08^{+0.15}_{-0.17}$, and $\chi^2/\nu = 147/133$. The BB flux corresponds to $62.5 \pm 3.9\%$ of the total observed 0.3-10 keV flux. The fits of the WT spectral slices using this model show that the temperature of the BB component decreases with time. There are also some hints that the power-law component steepens with time; however, the values of the spectral slope for each spectrum are consistent within the error bars, probably due to the poor statistics of the spectra at later times. The value of $\beta = 1.87^{+0.39}_{-0.62}$ in Table 4 was obtained by tying the spectral slope to the same value for each spectrum. The PC spectrum from the beginning of flare F₃ (from ~ 355 s to ~ 415 s) is well fit with a single power-law with $\beta = 1.62^{+0.37}_{-0.35}$ ($\chi^2/\nu = 5/9$); adding a BB component for this spectrum does not improve the fit significantly ($\Delta\chi^2 = 1.4$ for 2 dof). For the PC data from ~ 625 s to ~ 789 s, if we fix the spectral slope of the power-law to the mean slope obtained for WT spectra $\beta = 1.87$, then we can constrain the temperature of the black body (see Table 3).

Using a BBODYRAD model allows us to constrain the X-ray emitting radius of the black-body component, which increases from $R_X^i \sim 2.6^{+0.9}_{-0.6} \times 10^{13} \times \left(\frac{D_L}{20 \text{ Gpc}}\right)$ cm at the time interval 417-431s to $R_X^f \sim 9.8^{+1.8}_{-1.9} \times 10^{13} \times \left(\frac{D_L}{20 \text{ Gpc}}\right)$ cm at the time interval 471-501s, where D_L is the luminosity distance. We normalise to $D_L = 20$ Gpc, the luminosity distance for the average redshift ($z \sim 2.5$) for *Swift* GRBs. At later time, the emission radius is no longer well constrained. The results are summarised in Table 4.

Assuming that the shell of matter moves relativistically, the variation of the emission radius in the “thin shell” case is given by:

$$\Delta R(z) \equiv R_X^f(z) - R_X^i(z) = \frac{2c}{(1+z)} [t_f \Gamma^2(t_f) - t_i \Gamma^2(t_i)] \quad (1)$$

where z and c are the redshift and the velocity of light, respectively. Here, we define $t_{i,f}$ as the mean times of the time intervals 417-431s and 471-501s respectively. Fig. 7 shows the two parts of Eq. 1 as a function of the redshift assuming that the Lorentz factor γ has reached its coasting value. From the two plots, it seem more likely that the shell is

mildly relativistic ($\gamma < 10 - 15$). Otherwise, the solution of the above equation would require an unreasonable high redshift ($\gamma = 100$ would require a redshift much larger than 6).

From the PC data beyond 800 s, five spectra were extracted (see Table 3). The spectra from $\sim 4 \times 10^5$ s to $\sim 2 \times 10^6$ s were fit using Cash statistics due to the low number of counts in the spectra. The spectral slopes before and after the break in the light curve at $\sim 1.7 \times 10^4$ s are consistent within the error bars (see Table 3 and the HR plot in the bottom panel in Fig. 4). No clear spectral variation is seen around the time when the late X-ray bump occurred (around 1.1×10^5 s).

4. Discussion

We established in Section 3 that the burst 050822 is an XRF or an XRR GRB. Its X-ray light curve shows a steep-to-flat-to-steep decay. At least three X-ray flares peaking around $T_0 + 131$ s (F_1), 236 s (F_2) and 420 s (F_3) are superposed on the initial steep decay. A strong spectral evolution is observed during the flares. Flares F_2 and F_3 are best fit by broken power law spectral models, and we showed that the spectral softening during the decaying part of the flares is probably due to the shift of the energy peak of the spectrum (E_p) to lower energies. Interestingly, we found that the data for the X-ray flare F_3 are also well fit by a black-body plus power-law model as in the case of GRB 060218, the black-body component cooling down and expanding with time.

We discuss the possible origin of the X-ray flares in the framework of the internal shock model, which is often invoked to interpret the X-ray flares (e.g. Zhang et al. 2006, King et al. 2005).

The X-ray light curve also shows a long smooth decay from $\sim 1.7 \times 10^4$ s to $\sim 4 \times 10^6$ s without any evidence for a jet break. We investigate whether it is consistent with the prediction of the current afterglow models. We also discuss the possible origins of the late X-ray bump around $T_0 + 1.1 \times 10^5$ s and its implications.

4.1. The origin of the X-ray flares

The two early X-ray flares peaking around $T_0 + 236$ s (F_2) and 420 s (F_3) clearly show a positive correlation between brightness and spectral hardness i.e. higher the count rate is and harder the spectrum is (see the bottom panel in Fig. 4), as found for instance by Ford et al. (1995) in GRB pulses. We also note that the temporal profiles of the X-ray flares are well fitted by common FRED pulse shape (see Liang et al. 2006). The spectral softening seen for the X-ray flares can be explained by a shift of the energy peak to lower energy through the XRT energy band. This is clearly seen for the X-ray flare F_3 , for which the data are well fit by an absorbed broken power-law (see Fig. 6 and Table 3).

Indirect evidence for the shift of the peak energy to lower energies is also presented for the two other X-ray flares in Table 3.

Internal shocks - The presence of the energy peak in the XRT energy band is consistent with the internal shock model, as shown by Zhang & Mészáros (2002). In this model, the peak energy E_p of the synchrotron emission satisfies:

$$E_p \propto L^{1/2} \Gamma^{-2} \delta t^{-1}$$

where L and δt are the luminosity and the variability timescale, respectively. A smaller luminosity and/or a higher value of Γ and δt produces X-ray flares rather than Gamma-ray peaks. Here, the δt -values of the flares are larger than those of the Gamma-ray peaks. A longer duration of the X-ray flares is indeed expected at later times due to longer accretion episodes around the central new-born compact object (e.g. Perna et al. 2005 and Proga & Zhang 2006). It is not completely clear if the late Γ are higher or not. We could speculate that the late ejected shells interacting with a cleaner environment along the jet axis have higher Γ . It is nevertheless more likely that the main factor to produce a lower E_p is a smaller luminosity at later time. The shift of E_p in X-ray flares through the XRT energy band has also been reported in other *Swift* bursts (e.g. GRB 051117A, Goad et al. 2006). These authors also concluded that the X-ray flares are produced by internal shocks.

The low energy spectral slope ($\beta_1 = 1.06^{+0.16}_{-0.17}$) for the X-ray flare F₃ is steep compared to the mean values of the β_1 distribution derived from a sample of averaged time GRBs and XRFs ($\beta_1 \sim 0$; see Preece et al. 2000 and Kippen et al. 2003). The steep β_1 -value could suggest that the X-ray emission is not produced solely by synchrotron radiation, since the low energy spectral slope from shock accelerated electrons is expected to be between $-\frac{1}{3}$ and $\frac{1}{2}$ (e.g. Katz 1994, Cohen et al. 1997, Lloyd & Petrosian 2000).

Photospheric emission - In Section 3.3.2, we showed that the spectra of the X-ray flare F₃ are alternatively well fit by a black-body plus power-law model. According to the internal shock model, a quasi thermal spectrum is expected to be produced by pair photospheric emission from an optically-thick shocked shell of matter becoming optically thin at a radius R_τ . However, Comptonisation of the photospheric emission during the emergence of the spectrum (Goodman 1986, Ryle et al. 2006, Thompson et al. 2006) or a strong magnetic component could lead to a non-thermal tail in the spectrum (Thompson 1994; Mészáros & Rees 2000; Mészáros et al. 2002; Rees & Mészáros 2005). It is difficult to know whether or not the spectrum would peak in the XRT band, since it depends on the pair optical depth and the pair temperature (e.g. Zhang & Mészáros 2002). We note that Pe’er et al. (2006) concluded that energy peaks below a few keV are not expected in that picture. However, the parameters used in that paper were for the prompt emission. It could be possible that for plausible X-ray flare parameters, the photospheric

thermal component may be as low as keV or less (although more detailed modeling is needed, which is outside the scope of our paper). Finally, if the flare F_3 is produced by photospheric emission, the shell of matter producing the radiation needs to be mildly relativistic assuming that the shell already reached its maximum Lorentz factor ($\Gamma < 20$; see Section 3.2.2).

4.2. The X-ray light curve before $T_0 + 800$ s: the tail of the prompt emission

It is likely that the X-ray light curve before $T_0 + 800$ s is associated with the tail of the prompt emission: i) the X-ray flares are likely to be produced by internal processes; ii) curvature effect emission associated with the X-ray flares can account for the underlying decay seen in the X-ray light curve before $T_0 + 800$ s (see Section 3.1.2 and Liang et al. 2006); iii) the X-ray and Gamma-ray spectra from $T_0 + 111$ s to $T_0 + 125$ s are likely to be produced by the same physical mechanism (see Section 3.2.2).

4.3. Constraints on the evolution of the afterglow

The afterglow emergence - It is worth noting that a spectral hardening with time is clearly seen after $\sim T_0 + 700$ s in the WT and PC data (see the bottom panel in Fig. 4). Evidence that the X-ray continuum emission sometimes is harder during the shallow decay of the XRT light curves than during the initial steep decay has been found in several *Swift* bursts (e.g. O’Brien et al. 2006). The X-ray emission producing the initial steep decay and that producing the flat-to-steep decay were then interpreted as arising from different mechanisms (i.e. processes associated with the prompt emission, as discussed in Section 4.2, and external forward shock, respectively). We argue here that the spectral hardening seen after $\sim T_0 + 700$ s could be interpreted as the emergence of the forward-shock emission. If so, in the “thin shell” case, we could calculate a lower limit on the Lorentz factor from Eq. 10 in Zhang et al. (2006):

$$\Gamma \geq 100 \left(\frac{t_{\text{dec}}}{180 \text{ s}} \right)^{-3/8} E_{\text{iso},52}^{1/8} \left(\frac{\eta}{0.2} \right)^{-1/8} n^{1/8} \left(\frac{1+z}{2} \right)^{3/8} \quad (2)$$

where t_{dec} is the deceleration time (here $t_{\text{dec}} \sim 700$ s). $E_{\text{iso},52} = \frac{E_{\text{iso}}}{10^{52} \text{ erg}}$, η and n are the isotropic energy of the burst, the efficiency for the conversion of kinetic energy into gamma-rays and the CSM density, respectively. Assuming that the burst follows the Amati relation (Amati et al. 2002) and $E_p < 15$ keV (see Section 3.2.1), the isotropic energy should be less than $E_{\text{iso}} < 3 \times 10^{50} (1+z)^2$ erg. Since Γ in Eq. 2 depends weakly on η and n , we obtain a value of $\Gamma \geq 30 \times (1+z)^{5/8}$. This would give a minimum deceleration radius of $R_{\text{dec}} \sim 2 c t_{\text{dec}} \frac{\Gamma^2}{(1+z)} \geq 4 \times 10^{16} (1+z)^{9/8}$ cm. The inferred radius is much larger than the radius usually thought for the production of the internal shocks ($10^{13} - 10^{14}$ cm). The site of the emission after $T_0 + 700$ s is therefore different to that producing the emission before $T_0 + 700$ s.

Standard afterglow model - If the blast-wave evolution has already entered the slow cooling regime when deceleration started (i.e. $\nu > \max(\nu_m, \nu_c)$ where ν_m and ν_c are the synchrotron and cooling frequency respectively), then the temporal decay index (α) and the spectral slope (β) after the break at $\sim 1.7 \times 10^4$ s, are predicted to be $\alpha = (3p-2)/4$ (a) and $\beta = p/2$ (b) according to the CSM model (e.g. Sari et al. 1998) and the wind model (e.g. Chevalier & Li 2000), where p is the power law index of the electron distribution. We find $p = 2.22 \pm 0.18$ using (b) and $p = 2.07 \pm 0.07$ using (a). These values are consistent with the commonly used values of $p = 2.0 - 2.4$ (e.g. Kirk et al. 2000, Achterberg et al. 2001).

The shallow decay from $\sim T_0 + 800$ s to $\sim 1.7 \times 10^4$ s can then be interpreted as a phase of energy injection in the blast-wave, possibly due to a longer activity phase of the central engine (such as the kinematic luminosity $L \propto t^{-q}$) or a wide distribution of ejecta Lorentz factors (Rees & Mészáros 1998; Zhang & Mészáros 2001; Nousek et al. 2006; Zhang et al. 2006). In the case where $\nu > \max(\nu_m, \nu_c)$, we find $q = 0.32 \pm 0.15$, which is consistent with previously determined q -values (e.g. Zhang et al. 2006).

4.3.1. Any evidence for a jet break ?

The X-ray light curve of GRB 050822 after $T_0 + 1.7 \times 10^4$ s shows a monotonic, relatively smooth (except the late bump around 1.1×10^5 s) and long decay up to $T_0 + 4 \times 10^6$ s. No indication of any jet break is seen.

Fig. 8 shows the expected observed jet break time (t_{jet}) for different values of the observed energy peak (E_p^{obs}) as a function of the redshift z , using the relations from Amati et al. (2002; A02) and Liang & Zhang (2005; LZ05). Note that the LZ05 relation was originally established for optical breaks. However, if the jet models are correct, then the jet break time in the X-ray band should be the same. From the figure, it appears that whatever the values of z and E_p are, a jet break is expected in the light curve within the first 10 days after the burst. No such break is seen. A similar result was found in GRB 050416A (an XRF; Sakamoto et al. 2006), for which the A02 and LZ05 relations were inconsistent with the lack of a jet break up to $T_0 + 34.5$ days.

We discuss in the next Section whether the apparent absence of jet break in the light curve can be understood in the framework of the current jet models.

4.3.2. The jet models

The model of the off-axis uniform jet with the line-of-sight outside the jet edge (e.g. Yamazaki et al. 2003) can be ruled out. Indeed, this model predicts an initial fast rise when the emitting surface enters the line-of-sight of the observer followed by a rapid decay with $\alpha \sim p$ (e.g. Granot et al. 2002, 2005). This model is inconsistent with our data.

We can also rule out the model of the two-component jet with the line of sight on or close to the less energetic wider beam, because it does not account for all the Gamma-ray and X-ray properties seen for the burst.

GRB 050416A also has a very long power-law decay in its X-ray light curve, with no indication of a jet break. Mangano et al. (2006) have modelled the X-ray light curve of GRB 050416A using two jet models: (1) an on-axis uniform jet with a very wide opening angle (e.g. Lamb et al. 2005); (2) a structured Gaussian-like jet with the line of sight outside the bright Gaussian core (Zhang et al. 2004). We can infer from their Figure 5 that either of these jet models could work in the case of GRB 050822. In the case of the on-axis uniform jet model, the lack of a jet break in GRB 050822 requires a large jet half-opening angle (up to $\theta > 20^\circ$).

4.3.3. Origin of the late X-ray bump around $T_0 + 1.1 \times 10^5$ s

We next consider whether the X-ray bump around $t_{\text{bump}} = T_0 + 1.1 \times 10^5$ s could be produced by external shocks. Indeed, it has been proposed that abrupt density fluctuations in the circumburst medium can produce a significant re-brightening in the GRB afterglows via external shocks (e.g. Lazzati et al. 2002). However, if the blast-wave is still in the relativistic regime, the flux at $\nu > \nu_c$ should not (or only very weakly) be affected by circumburst density fluctuations (e.g. Nakar et al. 2003). Recent works have shown that if the blast-wave is still in the relativistic regime after the interaction and $\nu > \nu_c$, then the decay slope α is expected to vary, but no re-brightening is expected to be seen in the X-ray light curves (Nakar & Granot 2006). So the bump around 1.1×10^5 s is unlikely to be produced by the result of the interaction of the blast-wave with some clouds of matter or density jumps.

From the quality of the data around t_{bump} , we could not completely rule out that the X-ray bump could be produced by inhomogeneity in the blast-wave or by energy injection when we compare the rising ($0.2 < \delta t_r / t_{\text{bump}} < 1$) and decaying timescales ($\delta t_d / t_{\text{bump}} \sim 1$) of the bump with the limits given in Fig. 1 in Ioka et al. (2005).

As an alternative, the bump around $T_0 + 1.1 \times 10^5$ s could be interpreted as due to late internal shocks. Although this is unusual, other GRBs have exhibited some late X-ray flares (up to 10^5 s) which were interpreted as due to internal shocks (e.g. GRB 050202B, Falcone et al. 2006 and GRB 050724, Campana et al. 2006c). The quality of the PC data around the X-ray bump do not allow us to rule out this interpretation.

5. Conclusion

GRB 050822 is an XRF showing a complex X-ray light curve: i) an initial steep decay with three major X-ray flares; ii) a flat decay from $T_0 + 800$ s to $T_0 + 1.7 \times 10^4$; iii) a long and steeper decay up to $T_0 + 3 \times 10^6$ s with a X-ray bump around $T_0 + 1.1 \times 10^5$ s.

We argue that the three X-ray flares observed during the initial steep decay are likely to be produced by internal processes, and that the global decay is likely to be the tail of the prompt emission. We showed that the energy peak of the spectrum for the flare peaking around $T_0 + 420$ s is in the XRT energy band and shifts at lower energy with time. For the flares peaking at $T_0 + 131$ s and $T_0 + 236$ s, we showed that E_p is likely to be close to or less than the lower end of the XRT energy band.

Interestingly, the flare F_3 is alternatively well fit by a black-body + power-law (BB-PL) model. We then proposed that the flare F_3 could be produced by photospheric emission (involving Comptonisation) for a shell of matter moving at a mildly relativistic speed.

We stress that the spectral hardening seen around $\sim T_0 + 700$ s (close to the beginning of the flat decay) can be interpreted as a clear indication of the emergence of the forward-shock emission. We showed that the emission after $T_0 + 700$ s is then clearly produced in a site different to that producing the prompt emission, since the deceleration radius should be larger than 4×10^{16} cm.

The flat-to-steep decay can then be interpreted as being the afterglow, the flat part corresponding to a phase of energy injection. The null detection of a jet break up to $T_0 + 3 \times 10^6$ s in the X-ray light curve can be understood: i) if the jet seen on-axis is uniform with a large opening angle ($\theta > 20^\circ$); ii) if the jet is a structured Gaussian-like jet with the line-of-sight outside the bright Gaussian core. We note that the same models were also invoked in the case of GRB 050416A, which is an XRF (Mangano et al. 2006) to explain the null detection of a jet break in the light-curve. In both scenarii, the late X-ray bump around $T_0 + 1.1 \times 10^5$ s could be produced by internal shocks, implying a very late activity of the central source or it could be produced by inhomogeneity in the blast-wave or by energy injection.

OG, KPA, MRG, APB, JPO gratefully acknowledge PPARC funding. DNB, AF, JR and DCM are funded through NASA contract NAS5-00136.

References

- Abbey, T., Stevenson, T., Ambrosi, R. 2005, Proceeding of the “X-ray Universe” Conference, El Escorial Spain,
- Achterberg, A. et al., 2001, MNRAS, 328, 393
- Amati, L., et al., 2002, A&A, 390, 81
- Arnaud, K., 1996, in Jacoby G. Barnes., eds, *Astronomical Data Analysis Software and Systems*, ASP Conf. Series, 101, 17
- Band, D. et al., 1993, ApJ, 413, 281
- Barraud, C. et al., 2003, A&A, 400, 1021
- Barthelmy, S. et al., 2005, Space Sci. Rev., 120, 143
- Blustin, A. et al., GCN Circ. 3307 (2005)

- Burrows, D. N. et al., 2005, *Space Sci. Rev.*, 120, 165
- Butler, N. R., 2006, accepted to *ApJ*, astro-ph/0611031
- Campana, S. et al., 2006a, *Swift* XRT Response file release note
- Campana, S. et al., 2006b, *Nature*, accepted, astro-ph/0603279
- Campana, S. et al., 2006c, *A&A*, 454, 113
- Cash, W., 1979, *ApJ*, 228, 939
- Chevalier, R. A. & Li, Z.-Y., 2000, *ApJ*, 536, 195
- Churazov, E. et al., 1996, *ApJ*, 471, 673
- Cohen, E. et al., 1997, *ApJ*, 488, 330
- Dermer, C., 2004, *ApJ*, 614, 284
- Dermer, C. D., & Mitman, K. E., 2004, in *ASP Conf. Ser.* 312, Third Rome Workshop on Gamma-Ray Bursts in the Afterglow Era, ed. M. Feroci, F. Frontera, N. Masetti & L. Piro (San Francisco: ASP), 301
- Dermer, C. D. et al., 1999, *ApJ*, 513, 656
- Dickey, J. M. & Lockman, F. J., 1990, *ARA&A*, 28, 215
- Falcone, A. D. et al., 2006, *ApJ*, 641, 1010
- Ford, L. A. et al., 1995, *ApJ*, 439, 407
- Gehrels, N. et al. 2004, *ApJ*, 611, 1005
- Goad, M. R. et al., 2006, submitted to *A&A*, astro-ph/0612661
- Goodman, J., 1986, *ApJ*, 308, L47
- Granot, J. et al., 2005, *ApJ*, 630, 1003
- Granot, J. et al., 2002, *ApJ*, 570, L61
- Heise, J. et al., 2001, in *Proc. 2nd Rome Workshop: Gamma-Ray Bursts in the Afterglow Era*, ed. E. Costa, F. Frontera & J. Hjorth (Berlin: Springer), 16
- Hill, J. E. et al., 2005, *Proceedings of the SPIE*, in press
- Hill, J. E. et al., 2004, *Proceedings of the SPIE*, 5165, 217
- Huang, Y. F. et al. 2002, *MNRAS*, 332, 735
- Ioka, K., Kobayashi, S. & Zhang, B., 2005, *ApJ*, 631, 429
- Katz, J. I., 1994, *ApJ*, 432, L107
- King, A., O'Brien P. T., Goad, M. R., Osborne, J., Olsson, E., Page, K. P., 2005, *ApJ*, 630, 113
- Kirk, J. G. et al., 2000, *ApJ*, 542, 235
- Kippen, R. M. et al., 2003, in *AIP Conf. Proc.* 662, Gamma-Ray Burst and Afterglow Astronomy 2001, ed. G. R. Ricker & R. K. Vanderspek (New York: AIP), 244
- Krimm, H. Parsons, A. M. & Markwardt, C. B., 2004, *Swift BAT Ground Analysis Software Manual*
- Kumar, P. & Panaitescu, A., 2000, *ApJ*, 541, 51
- Lamb, D. Q. et al., 2005, *ApJ*, 620, 355
- Lamb, D. Q. et al., 2004, *NewA Rev.*, 48, 423
- Lazzati, D. et al., 2002, *A&A*, 396, 5
- Levan, A. J. et al., 2006a, accepted for publication in *ApJ*, astro-ph/0605256
- Levan, A. J. et al., 2006b, in preparation
- Li, L.-X., 2006, accepted for publication in *MNRAS*, astro-ph/0608315
- Liang, E. et al., 2006, *ApJ*, 646, 351

- Liang, E. & Zhang, B., 2005, *ApJ*, 633, 611
- Lloyd, N. M. & Petrosian, V., 2000, *ApJ*, 543, 722
- Mangano, V. et al., 2006, submitted to *ApJ*, astro-ph/0603738
- Mészáros, P. et al., 2002, *ApJ*, 578, 812
- Mészáros, P. & Rees, M. J., 2000, *ApJ*, 530, 292
- Mizuta, A. et al. 2006, accepted for publication in *ApJ*, astro-ph/0607544
- Mochkovitch, R. et al. 2004, in *ASP Conf. Ser.* 312. Third Rome Workshop on Gamma-Ray Bursts in the Afterglow Era, ed. M. Feroci, F. Frontera, N. Masetti & L. Piro (San Francisco: ASP), 381
- Moretti, A. et al., 2006, *A&A*, 448, L9
- Nousek, J. A. et al., 2006, *ApJ*, 642, 389
- O’Brien, P. T. et al., 2006, *ApJ*, 647, 1213
- Page, M. J. et al., 2005, *GCN Circ.* 3859
- Pe’er, A., Mészáros, P. & Rees, M. J., 2006, *ApJ*, 642, 995
- Perna, R., Armitage, P. J. & Zhang, B., 2005, *ApJ*, 636, 29
- Preece, R. D. et al., 2000, *ApJ Supplement*, 126, 19
- Proga, D. & Zhang, B., 2006, *MNRAS*, 370, L61
- Rees, M. J. & Mészáros, P., 2005, *ApJ*, 628, 847
- Rees, M. J. & Mészáros, P., 1998, *ApJ*, 496, L1
- Romano, P. et al., 2006, *A&A*, 450, 59
- Roming, P. W. A. et al., 2005, *Space Sci. Rev.*, 120, 95
- Ryde, F. et al., 2006, *ApJ*, 652, 1400
- Rykoff, E. S. et al., 2005, *GCN Circ.* 3850
- Sakamoto, T., et al., 2006, *ApJ*, 636, 73
- Sakamoto, T., et al., 2005, *ApJ*, 629, 311
- Sari, R., Piran, T. & Narayan, R., 1998, *apJ*, 497, 17
- Schady, P. et al., 2006, *ApJ*, 643, 276
- Thompson, C., Mészáros, P. & Rees, M. J., 2006, submitted to *ApJ*, astro-ph/0608282
- Thompson, C., 1994, *MNRAS*, 270, 480
- Thomson, B., et al., 2004, *A&A*, 419, 21
- Tominga, N., et al., 2004, *ApJ*, 612, 105
- Vaughan, S. et al., 2006, *ApJ*, 638, 920
- Watson, D., et al., 2004, *ApJ*, 605, 101
- Yamazaki, R. et al., 2003, *ApJ*, 593, 941
- Zhang, B. et al., 2006, *ApJ*, 642, 354
- Zhang, B. et al., 2004, *ApJ*, 601, 119
- Zhang, B. & Mészáros, P., 2002, *ApJ*, 581, 1236
- Zhang, B. & Mészáros, P., 2001, *ApJ*, 552, 35
- Zhang, W., Woosley, S. E., & Heger, A., 2004, *ApJ*, 608, 365

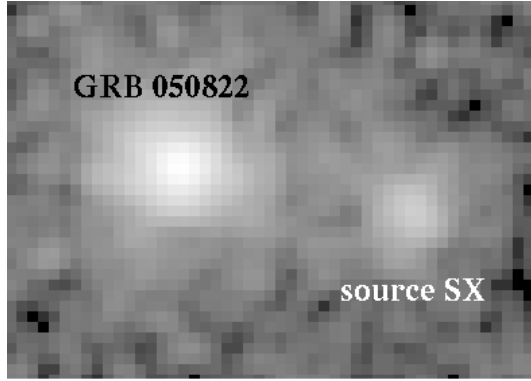


Fig. 1. 0.2-10 keV Photon Counting image of the sky region around the X-ray counterpart of GRB 050822 accumulated over 256 ks. The image is smoothed using a Gaussian with the value of the kernel radius fixed at 2. The nearby source SX is $4.9''$ away from the X-ray counterpart of GRB 050822 (see text).

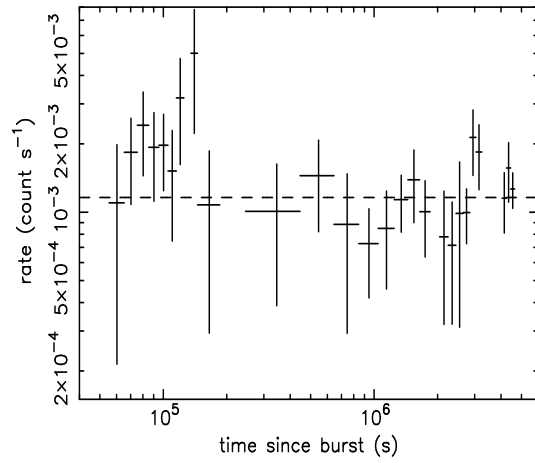


Fig. 2. 0.3-10 keV X-ray light curve of the X-ray source close to the position of GRB 050822. The light curve is extracted from $\sim 5 \times 10^4$ s to $\sim 5 \times 10^6$ s using a 15 pixel-radius extraction region.

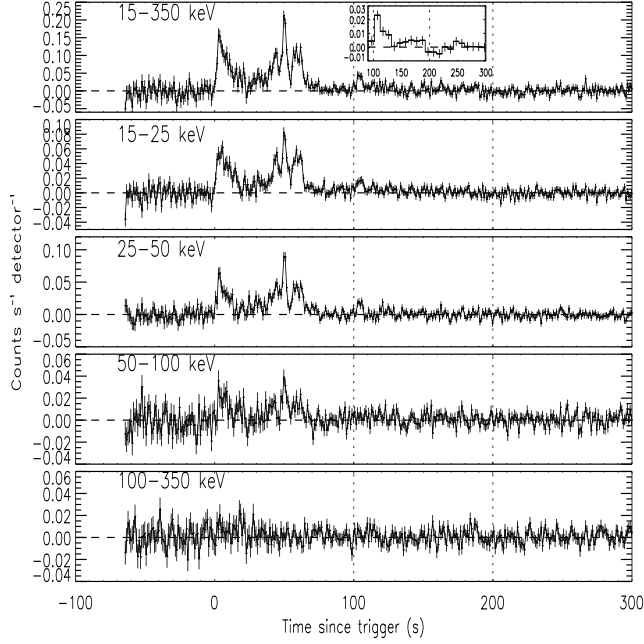


Fig. 3. Background-subtracted BAT light curve in units of count s^{-1} (fully illuminated detectors) $^{-1}$ for 4 different energy bands from the top to the bottom: 15-350 keV, 15-25 keV, 25-50 keV, 50-100 keV and 100-350 keV. The bin time is 1 s. The dashed vertical lines delimit the temporal interval where the BAT and XRT data overlap. In the small window using a bin time of 10 s, we show the late small flare between 100 s and 104 s and a possible tail up to $T_0 + 200$ s.

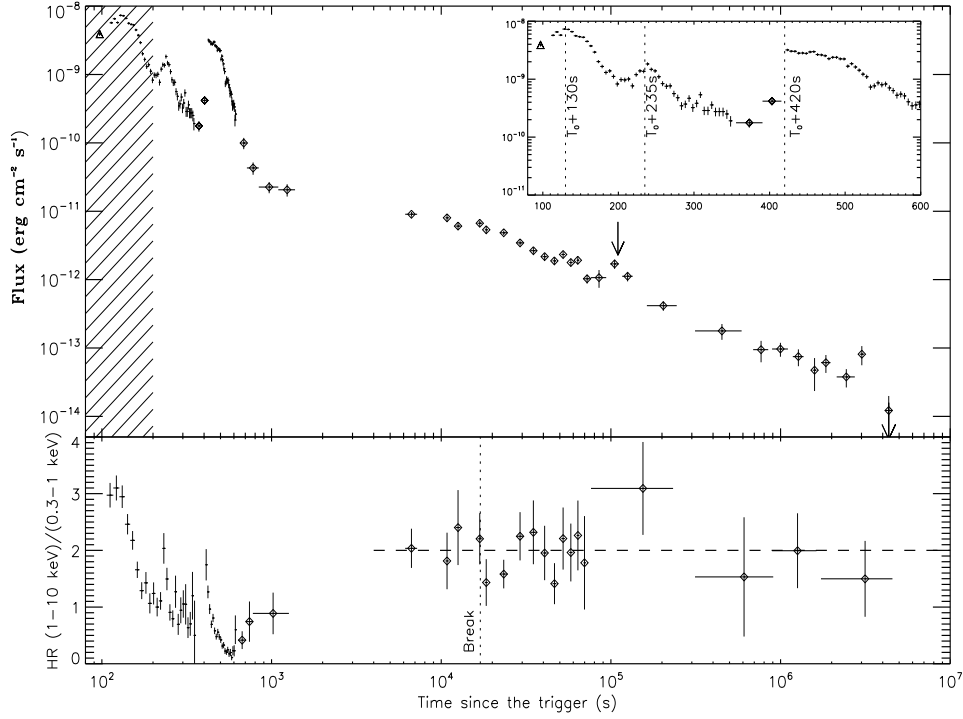


Fig. 4. Background subtracted XRT light curve of GRB 050822 in the 0.3-10 keV energy band in units of flux (top panel): IM data (triangle); WT data (crosses); PC data (diamonds). The upper limits are given at 3σ . The times of the early X-ray flares are shown in the inset. The hatched area corresponds to the temporal BAT/XRT overlap. The arrow around 1.1×10^5 s shows a possible late X-ray bump (see text for more details). (Bottom panel) Hardness ratio of GRB 050822 of the 1-10 keV band over the 0.3-1 keV band as a function of time. The error bars are 1σ statistical errors. The diamonds correspond to the PC data and the crosses to the WT data. The vertical dotted line represents the break seen in the X-ray light curve (see Section 3.2.2). The dashed line is the mean value of the hardness ratio beyond $T_0 + 1000$ s. Note that for the HR plot, we did not include the piled-up PC data from 354 s to 414 s and from 617 s to 690 s.

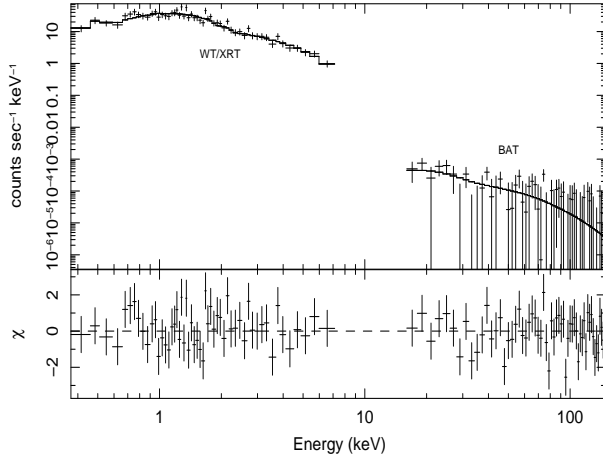


Fig. 5. Joint fit of the BAT/XRT spectra. The model is an absorbed power-law.

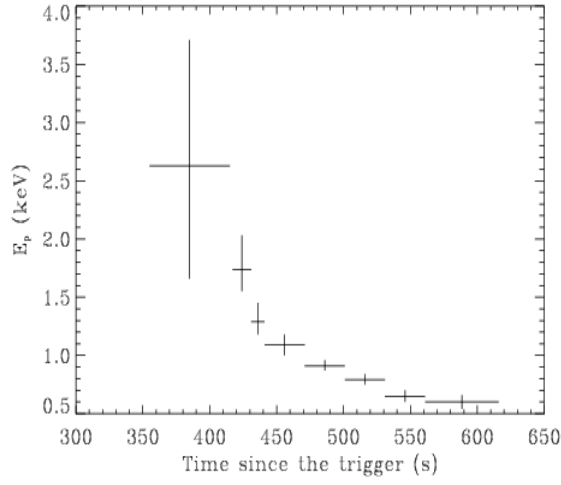


Fig. 6. Evolution of the peak energy during flare F_3 as a function of time, for a broken power-law spectral model.

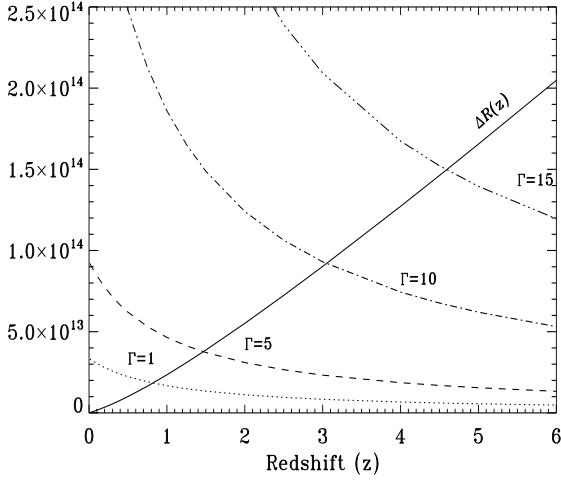


Fig. 7. Evolution of the two parts of Eq. 1 as a function of the redshift (z) assuming that the Lorentz factor γ has reached its coasting value. The intersections between the dotted and thick lines indicate the possible z -solutions for Eq. 1. The two parts of Eq. 1 are expressed in units of cm.

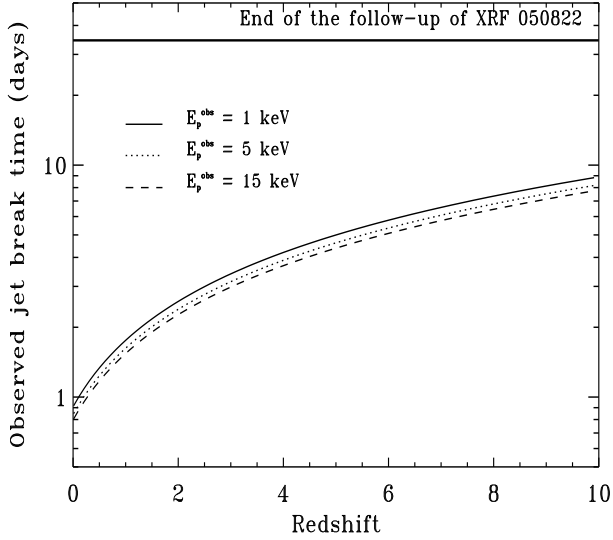


Fig. 8. Evolution of the jet break time as a function of the redshift for three values of the observed peak energy E_p^{obs} . The curves are deduced from the combination of the Amati et al. (2002) relation and Eq. 5 in Liang & Zhang (2005). The thick, solid line corresponds to the end of the XRT follow-up.

Table 1. Log of the XRT observations for GRB 050822 following the XRT mode sequence.

Sequence	XRT Mode	Start time (yy-mm-dd hh:mm:ss)	End time (yy-mm-dd hh:mm:ss)	Start time since trigger (s)
00151486000	IM	2005 – 08 – 22 03 : 51 : 04	2005 – 08 – 22 03 : 51 : 07	95
00151486000	WT	2005 – 08 – 22 03 : 51 : 20	2005 – 08 – 22 03 : 55 : 22	111
00151486000	PC	2005 – 08 – 22 03 : 55 : 23	2005 – 08 – 22 03 : 56 : 23	354
00151486000	WT	2005 – 08 – 22 03 : 56 : 26	2005 – 08 – 22 03 : 59 : 45	417
00151486000	PC	2005 – 08 – 22 03 : 59 : 46	2005 – 08 – 22 15 : 28 : 27	617
00151486001	PC	2005 – 08 – 22 16 : 23 : 49	2005 – 08 – 23 00 : 54 : 34	45260
00151486002	PC	2005 – 08 – 23 01 : 01 : 53	2005 – 08 – 23 17 : 08 : 59	76344
00151486003	PC	2005 – 08 – 24 01 : 05 : 26	2005 – 08 – 24 23 : 40 : 58	162957
00151486004	PC	2005 – 08 – 25 11 : 41 : 57	2005 – 08 – 25 23 : 35 : 57	287548
00151486005	PC	2005 – 08 – 27 20 : 35 : 26	2005 – 08 – 28 23 : 34 : 13	492357
00151486006	PC	2005 – 08 – 30 03 : 17 : 39	2005 – 08 – 30 22 : 42 : 58	689290
00151486007	PC	2005 – 08 – 31 07 : 49 : 39	2005 – 08 – 31 22 : 44 : 58	792010
00151486008	PC	2005 – 09 – 01 11 : 22 : 21	2005 – 09 – 01 21 : 18 : 57	891172
00151486009	PC	2005 – 09 – 02 00 : 26 : 17	2005 – 09 – 03 22 : 44 : 13	938208
00151486010	PC	2005 – 09 – 04 19 : 48 : 16	2005 – 09 – 06 04 : 03 : 57	1180727
00151486011	PC	2005 – 09 – 09 01 : 11 : 27	2005 – 09 – 09 23 : 57 : 58	1545718
00151486012	PC	2005 – 09 – 11 04 : 44 : 06	2005 – 09 – 12 22 : 42 : 58	1731277
00151486013	PC	2005 – 09 – 13 00 : 05 : 00	2005 – 09 – 13 22 : 39 : 57	1887331
00151486014	PC	2005 – 09 – 15 00 : 05 : 59	2005 – 09 – 15 22 : 53 : 31	2060190
00151486015	PC	2005 – 09 – 17 00 : 13 : 10	2005 – 09 – 18 06 : 52 : 57	2233421
00151486016	PC	2005 – 09 – 21 00 : 43 : 48	2005 – 09 – 22 07 : 16 : 58	2580859
00151486018	PC	2005 – 09 – 23 16 : 47 : 12	2005 – 09 – 26 23 : 59 : 58	2822463
00151486020	PC	2005 – 10 – 08 18 : 52 : 01	2005 – 10 – 10 17 : 34 : 11	4114952
00151486021	PC	2005 – 10 – 12 05 : 53 : 30	2005 – 10 – 12 23 : 59 : 57	4413841
00151486022	PC	2005 – 10 – 13 01 : 32 : 24	2005 – 10 – 13 03 : 21 : 58	4484575

Table 2. Summary of the Gamma-ray spectral fitting parameters.

Time interval since T_0	β	$\chi^2(dof)$	Fluence* ($\times 10^{-6}$ erg cm $^{-2}$)
0 - T_{50}	1.36 ± 0.16	47 (56)	$1.4^{+0.2}_{-0.3}$
T_{50} - 110 s	1.63 ± 0.25	49.4 (56)	0.9 ± 0.2
0 - 110 s	$1.46^{+0.15}_{-0.14}$	55.5 (56)	$2.4^{+0.2}_{-0.3}$
90 - 125 s	$1.57^{+0.73}_{-0.57}$	53.4 (56)	0.2 ± 0.1

*The fluences are given in the 15-150 keV energy range.

Table 3. Summary of the X-ray spectral parameters for the best models. Note that we use two WABS models fixed to the Galactic value ($N_H^{Gal} = 2.34 \times 10^{20} \text{ cm}^{-2}$) and to the value of excess absorption ($\Delta n_H(z=0) = 1.2 \times 10^{21} \text{ cm}^{-2}$). The symbols F_n correspond to the three X-ray flares peaking around $T_0 + 131 \text{ s}$ (F_1), 236 s (F_2) and 420 s (F_3) as defined in Section 3.2.2.

XRT mode	Time interval since T_0	Model	Flux [†]	$\chi^2(\nu)$	Model	Flux [†]	$\chi^2(\nu)$
Power-law							
WT1(F_1)	111 - 121 s	0.80 ± 0.10	$9.43^{+0.69}_{-0.65}$	21.2 (31)			
WT2(F_1)	121 - 131 s	0.79 ± 0.11	$8.46^{+0.60}_{-0.43}$	21.9 (28)			
WT3(F_1)	131 - 145 s	0.88 ± 0.08	$9.04^{+0.40}_{-0.49}$	42.4 (44)			
WT4(F_1)	145 - 161 s	1.08 ± 0.09	$6.86^{+0.35}_{-0.39}$	34.4 (39)			
WT5(F_1)	161 - 181 s	1.47 ± 0.13	$3.43^{+0.20}_{-0.18}$	36.8 (24)			
WT6(F_1)	181 - 211 s	$1.63^{+0.20}_{-0.19}$	$1.61^{+0.11}_{-0.13}$	23.6 (16)			
Broken power-law							
$\beta_1 = 0$ fixed							
WT7(F_2)	211 - 236 s	$E_p < 0.75 \text{ keV}$	$1.47^{+0.14}_{-0.30}$	10.6 (12)			
$\beta_2 = 1.72^{+0.23}_{-0.20}$							
WT8(F_2)	236 - 261 s	$E_p = 0.83^{+0.12}_{-0.15} \text{ keV}$	$1.51^{+0.15}_{-0.16}$	5.3 (13)			
$\beta_2 = 1.88^{+0.33}_{-0.30}$							
WT9(F_2)	261 - 301 s	$E_p < 0.65 \text{ keV}$	$0.69^{+0.03}_{-0.62}$	20.9 (17) [‡]			
$\beta_2 = 2.02^{+0.48}_{-0.29}$							
Power-law							
WT10(F_2)	301 - 351 s	$1.99^{+0.23}_{-0.22}$	$0.48^{+0.08}_{-0.07}$	109 (111)*			
Broken power-law							
$\beta_1 = 1.06^{+0.16}_{-0.17}$							
$\beta_2 = 4.09^{+0.25}_{-0.21}$							
E_p (keV)							
PC(F_3)	355 - 415 s	$2.63^{+1.08}_{-0.97}$	0.19 ± 0.04	5.1 (9) [‡]	PL+BB ^a		
$\beta = 1.87^{+0.39}_{-0.62}$							
WT11(F_3)	417 - 431 s	$1.74^{+0.29}_{-0.19}$	$2.11^{+0.18}_{-0.15}$	181.1 (201)	0.29 ± 0.04	$2.09^{+0.34}_{-0.23}$	159 (195)
WT12(F_3)	431 - 441 s	$1.29^{+0.16}_{-0.11}$	$2.38^{+0.19}_{-0.22}$	-	0.23 ± 0.03	$2.48^{+0.42}_{-0.39}$	-
WT13(F_3)	441 - 471 s	$1.09^{+0.09}_{-0.09}$	2.27 ± 0.13	-	0.19 ± 0.01	$2.16^{+0.21}_{-0.12}$	-
WT14(F_3)	471 - 501 s	$0.91^{+0.05}_{-0.04}$	$2.12^{+0.15}_{-0.13}$	-	0.17 ± 0.01	$2.00^{+0.24}_{-0.11}$	-
WT15(F_3)	501 - 531 s	$0.79^{+0.05}_{-0.04}$	$1.68^{+0.15}_{-0.14}$	-	0.14 ± 0.01	$1.61^{+0.18}_{-0.16}$	-
WT16(F_3)	531 - 561 s	0.65 ± 0.05	$1.06^{+0.11}_{-0.15}$	-	0.12 ± 0.01	$1.06^{+0.15}_{-0.16}$	-
WT17(F_3)	561 - 616 s	0.60 ± 0.06	$0.47^{+0.05}_{-0.08}$	-	0.11 ± 0.01	$0.50^{+0.07}_{-0.11}$	-
Power-law							
PC(F_3)	625 - 789 s	$3.12^{+0.62}_{-0.58}$	$0.17^{+0.04}_{-0.03}$	15.8 (11) [‡]	$0.08^{+0.04b}_{-0.03}$	$0.16^{+0.08}_{-0.09}$	15 (10) [‡]
Power-law							
PC	$\sim 800 - \sim 4.1 \times 10^4 \text{ s}$	1.11 ± 0.09	$4.36^{+0.40}_{-0.40} \times 10^{-2}$	41.2 (47)			
PC	$\sim 800 - \sim 1.7 \times 10^4 \text{ s}$	1.12 ± 0.15	$7.18^{+0.98}_{-1.03} \times 10^{-2}$	19.5 (20)			
PC	$\sim 1.7 - 4.1 \times 10^4 \text{ s}$	1.11 ± 0.11	$3.24^{+0.33}_{-0.37} \times 10^{-2}$	30.8 (26)			
PC	$\sim 8 - 12.5 \times 10^4 \text{ s}$	$1.02^{+0.42}_{-0.37}$	$9.46^{+4.69}_{-4.60} \times 10^{-3}$	6.1 (7) [‡]			
PC	$\sim 0.4 - 2 \times 10^6 \text{ s}$	$0.98^{+0.45}_{-0.42}$	$6.87^{+3.87}_{-4.05} \times 10^{-4}$	62 (113)*			

[†] F is the unabsorbed flux given in the 0.3-10 keV energy band in units of ($\times 10^{-9} \text{ erg cm}^{-2}$)

Table 4. Summary of the emitting radius of the black-body component for the WT data fit from 417 s to 501 s.

Time interval since T_0	R_X ($\times 10^{13} D_{20 \text{ Gpc}} \text{ cm}$)
417-431 s	$2.6^{+0.9}_{-0.6}$
431-441 s	$4.4^{+1.2}_{-1.5}$
441-471 s	$6.9^{+0.8}_{-0.7}$
471-501 s	$9.8^{+1.8}_{-1.9}$

* $D_{20 \text{ Gpc}} = \frac{D_L}{20 \text{ Gpc}}$, where D_L is the luminosity distance of the source and 20 Gpc is the approximate luminosity distance of the mean *Swift* GRB redshift, using WMAP cosmology.